Bottom-up model of adsorption and transport in multiscale porous media

Alexandru Boţan, Franz-Josef Ulm, Roland J.-M. Pellenq, and Benoit Coasne*

MultiScale Materials Science for Energy and Environment, UMI 3466 CNRS-MIT, Massachusetts Institute of Technology, Cambridge, Massachusetts, USA

and Department of Civil and Environmental Engineering, Massachusetts Institute of Technology, Cambridge, Massachusetts, USA

(Received 8 January 2014; revised manuscript received 9 June 2014; published 20 March 2015)

We develop a model of transport in multiscale porous media which accounts for adsorption in the different porosity scales. This model employs statistical mechanics to upscale molecular simulation and describe adsorption and transport at larger time and length scales. Using atom-scale simulations, which capture the changes in adsorption and transport with temperature, pressure, pore size, etc., this approach does not assume any adsorption or flow type. Moreover, by relating the local chemical potential $\mu(\mathbf{r})$ and density $\rho(\mathbf{r})$, the present model accounts for adsorption effects and possible changes in the confined fluid state upon transport. This model constitutes a bottom-up framework of adsorption and transport in multiscale materials as it (1) describes the adsorption-transport interplay, (2) accounts for the hydrodynamics breakdown at the nm scale, and (3) is multiscale.

DOI: 10.1103/PhysRevE.91.032133 PACS number(s): 05.60.Cd, 47.56.+r, 68.43.−h, 81.05.Rm

I. INTRODUCTION

Fluid transport in porous media such as soils, rocks, and shales and materials such as concrete is of utmost importance [1–3]. A major difficulty in describing transport in these media stems from their multiscale porosity with a pore distribution spanning orders of magnitude (from <1 nm to the macroscopic scale). Transport in subnanopores (<1 nm) is diffusive (Fickian) or anomalous depending on the probed scale. Transport in nanopores (∼1−100 nm) and macropores (>100 nm) is diffusive, viscous (Darcy), or both (convective) depending on pressure and temperature [4]. For small pores (large surface-to-volume ratio), the situation is further complicated as transport can include Knudsen diffusion when the fluid mean free path is larger than the pore size [5,6]. Depending on the surface interaction, fluid slippage at the surface (Klinkenberg effect) can also occur [7,8]. Moreover, the fluid state in each pore must be considered; depending on temperature and pore size, the fluid is supercritical (reversible and continuous filling) or critical (capillary condensation). In the latter case, the pore is filled above the condensation pressure P_c or covered with an adsorbed film coexisting with the gas below P_c [9].

There are three bottlenecks to describe adsorption and transport in multiscale porous media.

(1) *Adsorption/transport interplay*: The rich and complex behavior of confined fluids, from reversible filling (small pores) to capillary condensation (large pores), induces phase transitions and interfaces between coexisting phases [9].

(2) *Hydrodynamics breakdown at the nm scale*: New phenomena (slippage, interfacial transport, and nonviscous effects) appear when the atom granularity becomes non-negligible [10].

(3) *Multiscale transport*: The flow, which results from the transport regimes coexisting in a multiscale medium (diffusive, viscous, molecular sieving, Knudsen, etc.), requires an upscaling technique that combines the different phenomena at each scale.

Available approaches do not offer the ground for a bottom up model of multiscale adsorption and transport because they describe empirically the adsorption-transport interplay, assume that hydrodynamics remains valid at the nm scale, and/or are not multiscale. Fluid mechanics such as computational fluid dynamics, which relies on Navier-Stokes and Boltzmann equations, is not suited as it assumes that the flow regime at the field scale remains valid at vanishing scales and does not account for adsorption and the wide range of confined fluid states [11–13]. Recently, Levesque *et al.* [14] have attempted to account for adsorption in the mesoscopic equations of lattice Boltzmann dynamics [15] while Albaalbaki and Hill have integrated adsorption in continuum models with diffusion processes [16]. Homogenization methods also allow inserting adsorption effects in transport at a given scale [17,18]. These techniques are valid at a given scale but they do not include transport responses to the many adsorption phenomena such as hysteretic condensation. In particular, they fail to account for the complex behavior of confined fluids such as possible interfaces between filled and empty pores and associated activated transport [19].

In addition to addressing the three key issues above, any approach of adsorption and transport in multiscale porous solids must capture both the complexity of the host material (chemical and structural heterogeneity, possibly covering a range of length and time scales) and the complex interaction of the mobile fluid with the porous material. Such an interaction between the fluid and the host solid modifies both the thermodynamics of the fluid, including possible phase transitions occurring locally due to the confining surfaces, and the resulting transport properties which depend among other variables on the local fluid density. The fluid-solid interactions in nanopores can only be captured correctly using molecular simulations, which fail to account for the complexity of the materials on larger scales. On the other hand, traditional approaches accounting for the latter rely on an oversimplified picture of the fluid and its transport properties.

In this paper, we present a novel bottom-up approach of multiscale adsorption and transport in porous media which captures the effects of adsorption and changes in the confined fluid state. This model employs a lattice model in

*coasne@mit.edu

which accurate molecular simulations are upscaled to predict transport on larger scales. The methodology can be upscaled several times from molecular to engineering scales without losing information at the lower scale. By relying on molecular dynamics (MD) simulations, which capture the changes in transport with temperature T, pressure P, concentration c, and pore size D, our approach does not require assuming any flow type (Darcy, diffusive, Knudsen, etc.). Moreover, by relating the local chemical potential $\mu(\mathbf{r})$ and density $\rho(\mathbf{r})$ using grand-canonical Monte Carlo (GCMC) simulations, the present model accounts for adsorption and possible changes in the confined fluid state which occur upon transport.

The remainder of this paper is organized as follows. After a brief state of the art, we first present our bottom-up model of adsorption and transport in multiscale media. Using a real multiscale porous structure corresponding to shale, our model is validated against Fick's second law (under appropriate conditions) before showing that the smallest porosity (<10 nm) accounts for the low permeability of such complex media. We then show that this model allows recovering Archie's empirical law [20] in which the flux in disordered porous media scales with porosity, $J \sim \phi^m$ (m usually between 1.8 and 2 [21]). By expressing J in terms of tortuosity τ (transport resistance), we show that τ can be written as the product of geometrical τ_{geo} and adsorption τ_{ads} contributions; while τ_{geo} is a simple power law of ϕ and can be assessed from random-walk simulations, τ_{ads} weakly depends on ϕ and accounts for nongeometric effects (e.g., slippage and adsorption).

II. MODEL AND METHODS

A. State of the art

Any multiscale approach must provide a framework to bridge scales in order to describe combined transport, mechanical, and structural properties of a given sample. If restricted to adsorption and transport, this implies to link accurate atomistic molecular dynamics simulations, pore scale methods such as lattice Boltzmann (LB) and dissipative particle dynamics (DPD), smoothed-particle hydrodynamics, and macroscopic models such as finite-element methods. Because MD simulations provide a means to simulate trajectories of atoms and molecules, it yields detailed information about the thermodynamical, structural, and dynamical properties of the confined fluid [22]. On the other hand, the system size that can be assessed using MD is limited to tens of nanometers and the simulation time does not exceed 1 μs at most.

Several attempts have been made to develop atomistic-to-continuum coupling methods [11,23–25] in which continuum equations are solved in homogeneous domains, while an atomistic description is used at interfaces between these domains [26]. These two descriptions are coupled in the interfacial region, therefore leading to an MD-continuum hybrid description. The boundary conditions that are used as inputs for solving the continuum equations are usually obtained by averaging the corresponding quantities over the local region and over time [25]. Another solution used to couple atom-scale simulations and continuum equations consists of extracting information such as slip length, adsorption isotherms, fluid permeability through micropores, etc., from molecular simulation for subsequent use in pore scale models. For instance, instead of considering the trajectory of individual molecules, the LB method describes the transport of fluid particles (molecule cluster) [27]. The motion and interactions of such particles are determined using equations based on the Boltzmann equation, which can be reduced to the Navier-Stokes equations. Fluid flow through micropores can be assessed using the LB method by using immersed boundary conditions [28] and/or "gray" LB techniques [29].

Dissipative particle dynamics also allows describing the adsorption and transport of fluid particles at the mesoscale [30]. DPD is a particle method in which molecules are grouped into beads in order to adopt a mesoscopic picture of fluid dynamics. Newton's second law is used to determine the dynamics of these particles subjected to repulsive, dissipative or frictional, and random forces. While the method used to probe the fluid dynamics in DPD resembles that in MD, the coarse-grained approach adopted in the former allows simulating the system on much larger length and time scales due to the reduced computational burden. The coarse-grained techniques above are interesting methods to probe mesoscale dynamics in porous media. However, they cannot be used at scales that are orders of magnitude larger than the pore scale due to their computational cost.

Continuum approaches allow overcoming the limitations above as they rely on phenomenological descriptions such as Darcy's law [31]. The coupling between scales is achieved using upscaling techniques known as homogenization procedures. The most common homogenization technique consists of upscaling from the pore scale to larger scales by averaging the pore scale transport over a representative volume to obtain a macroscopic transport model [32,33]. While such techniques describe empirically the coupling between adsorption and transport at a given scale, they necessarily fail to describe possible changes in the confined fluid state and its effect on transport. For instance, possible capillary condensation effects upon transport (induced as the local chemical potential reaches a specific value for a given pore size or scale) cannot be described using homogenization techniques in which a single density or pressure equation is used for a given type (therefore not accounting for possible adsorption changes induced by transport). It is worth mentioning that many works in the literature use hybrid models, which employ pore scale and continuum descriptions of the same phenomenon in different regions of a computational domain [34–37]. A number of other upscaling approaches have been reviewed in Refs. [38,39].

While the approaches above are valid for a given adsorption and transport regimes, they fail to capture the different thermodynamical and dynamical regimes occurring upon transport in multiscale porous media. For instance, a transition between diffusion in multilayer adsorption and nondiffusive, activated transport occurs upon condensation [19]. This shows that interfaces between filled and empty pores are energy barriers whose influence on transport remains to be understood. Another important phenomenon, which cannot be captured *a priori* by the approaches above, is the rich and complex behavior of confined fluids, including a shift of the critical temperature upon confinement. Indeed, experimental, theoretical, and molecular simulation works have shown that there is a temperature, the so-called capillary condensation

temperature T_{cc}, above which capillary condensation in porous solids becomes reversible [9]. This pseudocritical temperature corresponds to the threshold of reversible capillary condensation of the confined fluid. As the temperature approaches T_{cc} the hysteresis loop shrinks and disappears for $T = T_{cc}$. We also know that $T_{cc}(D)$ increases as the pore diameter D increases. Consequently, for a given temperature T, the hysteresis loop decreases as D decreases and eventually disappears when D is such that $T > T_{cc}(D)$. The different approaches above do not capture hysteretic condensation in pores as well as the shift of the critical point of confined fluids (which scales as the pore diameter D divided by the size σ of the adsorbate molecule). As stated earlier, by relying on both molecular dynamics and grand-canonical Monte Carlo simulations, which capture the different phenomena mentioned above, the model reported in the present paper allows us to take into account the different adsorption and transport regimes and their crossovers involved in multiscale porous media.

B. Multiscale model

The upscaling technique in our model requires two independent steps. The first step consists in atomic GCMC and MD simulations of adsorption and transport in different domains: subnano-, nano-, and macropores. For each domain type x, GCMC allows us to determine the fluid density $\rho_x(\mu)$ as a function of the chemical potential $\mu = \mu(P,T,c,\dots)$. $\rho_x(\mu)$ is then used in a lattice model of adsorption and transport to include local effects of adsorption and of the confined fluid state by estimating the local chemical potential from its density. MD is also performed to estimate for each domain type x the flux $\vec{J}$ induced by a chemical potential gradient $\vec{\nabla}\mu$. $\vec{J}$ is written in the frame of Onsager's theory which assumes a linear response:

$$\vec{J} = -M_x(\mu)\vec{\nabla}\mu, \tag{1}$$

where $M_x(\mu)$ is the transport coefficient (mobility) describing the fluid response in a domain type x. Transport is described as a response to $\vec{\nabla}\mu$ since any driving force ($\vec{\nabla}P$, $\vec{\nabla}T$, or $\vec{\nabla}c$) can be converted into $\vec{\nabla}\mu$. For simplicity, we consider here $\vec{\nabla}T = 0$ and pure fluids $\vec{\nabla}c = 0$ so $\vec{\nabla}P$ is related to $\vec{\nabla}\mu$ through the Gibbs-Duhem equation: $\rho d\mu = dP$. $|\vec{\nabla}P| = \rho|\vec{\nabla}\mu|$ for incompressible liquids ($\rho \sim$ constant) and $|\vec{\nabla}P|/P = \exp(L|\vec{\nabla}\mu|/k_BT)/L$ for ideal gases where L is the membrane length. For nonideal gases, P must be replaced by the fugacity $f = \tilde{f}P$ ($\tilde{f}$ is the fugacity coefficient). For parameters relevant to the experimental conditions such as T and P, $M_x(\mu)$ is estimated using grand-canonical molecular dynamics simulations [40].

The second step in our model consists in upscaling the GCMC-MD results into a lattice model to describe adsorption and transport at a larger scale. The lattice is mapped onto three-dimensional (3D) structures obtained using focused ion beam-scanning electron microscopy, tomography, etc., as shown in Fig. 1. The system is divided into a grid of equal-size tiles where each tile of a size l is a subnano-, nano-, or macroporous domain. Here subnano- and nanoporous domains are obtained by placing eight nonporous spheres of a radius $r = 1.0$ nm and 0.7 nm, respectively, in a cube of a size $a = 2.5$ nm. These domains are referred to as subnano- (S) and nano- (N) porous domains. We also consider subnanoporous domains (S') made of a realistic model of disordered porous carbons [41]. Macroporous domains (M) are assumed to obey bulk transport through the Maxwell-Stefan equation.

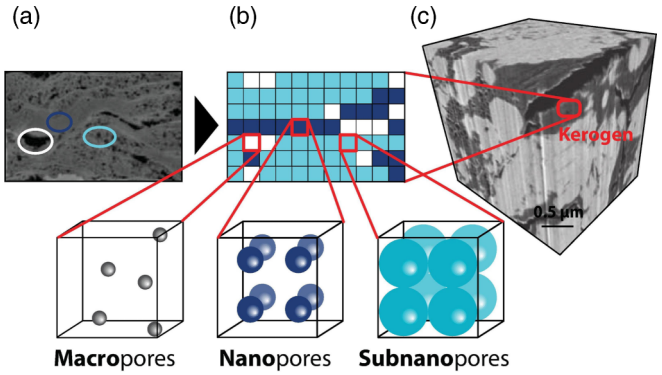

FIG. 1. (Color online) A lattice of equal-size tiles is mapped onto 3D data for an experimental sample (here gas shale). Each tile is a subnano- (cyan), nano- (dark blue), or macroporous (white) domain. While macroporous domains (M) are assumed to obey bulk transport, subnano- (S) and nano- (N) porous domains are obtained by placing eight nonporous spheres of a radius $r = 1.0$ nm and 0.7 nm in a cubic box of a size 2.5 nm. Subnanoporous domains (S') made of disordered porous carbon are also considered (not shown).

Once mapped on structural data, the lattice of a length L is used to solve transport when $\vec{\nabla}\mu = (\mu_\uparrow - \mu_\downarrow)/L$ is imposed across the system. To do that, an extra row of sites is added at each end of the lattice. These sites, which play the role of bulk reservoirs at the ends of the membrane, are assigned local chemical potentials $\mu_\uparrow$ and $\mu_\downarrow$. In all simulations, the temperature remains constant. The initial density at each site corresponding to a domain x ($x = S$, S', N, or M) is equal to the density given by the adsorption isotherm $\rho_x(\mu_\uparrow)$. In this configuration, starting from a membrane equilibrated at a chemical potential $\mu_\uparrow$, transport will be induced by setting the membrane in contact with a chemical potential $\mu_\downarrow$ at one of its extremities.

Starting from the equilibrated membrane at a time $t = 0$, each time step of the lattice simulation involves two steps. The change in the local density ρ_i for each site i is first computed by considering incoming and outgoing fluxes from and to adjacent neighbors:

$$\frac{d\rho_i}{dt} = -\sum_a J_{i\to i+a}(t) = \sum_a M_x(\mu_i)\frac{\mu_{i+a} - \mu_i}{l}. \tag{2}$$

The flux $J_{i\to i+a}$ from site i to adjacent site $i + a$ is estimated from the local chemical potential gradient $(\mu_{i+a} - \mu_i)/l$ using $M_x(\mu_i)$ (previously estimated from MD for each type x). Once the new local density $\rho_i = \rho$ is determined, the local chemical potential μ_i for each site i is updated by taking μ_i, which corresponds to $\rho_x(\mu) = \rho$ [we recall that $\rho_x(\mu)$ corresponds to the adsorption isotherm for a domain of type x]. Once a steady-state flow is reached, the flux J is calculated as the amount of fluid crossing the membrane per unit of time divided by the surface area of the lattice. As explained

in detail below, the following combination rule, which relies on time scales, was used: $J^{\alpha\beta} = 2J^{\alpha\alpha}J^{\beta\beta}/(J^{\alpha\alpha} + J^{\beta\beta})$. This constitutes an approximation of real systems in which adsorption at the interface between different domain types might affect transport. This approximation is valid for large domains where the effects of adsorption and dynamics at the external surface are negligible compared to phenomena occurring in the domain center. In case of much smaller domains, further work is needed to address the effect of adsorption between neighboring domains; interfacial effects can be accounted for by adding domains consisting of boundaries between different domains.

Local mass balance between two adjacent sites requires that $J_{i\to i+a} = -J_{i+a\to i}$. In our approach, the following combination rule automatically ensures local mass balance. Let $\tau_{\alpha\alpha} \sim 1/J_{\alpha\alpha}$ be the time required to transfer the fluid density over a site of type α of a length l when the local flux is $J_{\alpha\alpha}$. The time required to transfer the density from the middle of site α to the middle of site β is $\tau_{\alpha\beta} = \frac{1}{2}(J_{\alpha\alpha} + J_{\beta\beta}) \sim l/J_{\alpha\beta}$ so $J_{\alpha\beta} = 2J_{\alpha\alpha}J_{\beta\beta}/(J_{\alpha\alpha} + J_{\beta\beta})$. The latter combining rule ensures that $J_{i\to i+a} = -J_{i+a\to i}$ even if a and i are of different types. In particular, considering that the chemical potential gradient between i and a is the opposite of the chemical potential gradient between a and i ($\nabla_{ia} = -\nabla_{ai}$), the combining rule selected in this paper ensures that local mass balance is verified. We note that our approach is somehow equivalent to the usual strategy consisting of defining the mobility M as a property of the link between two cells rather than of the starting cell only. Such an approach has been proposed for the simulation of diffusion in heterogeneous materials, and a common choice for the diffusion coefficient of the link is to use the harmonic mean of the two diffusion coefficients of the cells [42]. A more complex example involving chemical potential gradient is the link-flux method introduced in Lattice-Boltzmann simulations by Capuani *et al.* [43].

C. Molecular simulation

The dual control volume grand-canonical molecular dynamics (DCV-GCMD) technique [44,45] is employed to study at the molecular level the flow induced by a chemical potential gradient through membranes. The simulation setup, which aims at emulating an experimental arrangement used for permeability measurements, is shown in Fig. 2. The simulation box consists of two reservoirs (two low-fugacity volumes, connected to each other because of the periodic boundary conditions, and one high-fugacity volume, where the chemical potentials are kept constant) and two membranes settled between the reservoirs. Fluid molecules permeate through the membranes from the high- to the low-fugacity reservoirs. The fugacity is simply related to the chemical potential using $\mu \sim k_B T \ln f$. The flow J can be estimated by counting the number N of molecules crossing the membrane having a surface area A over a time Δt,

$$J = \frac{N}{A\Delta t}. \tag{3}$$

The mobility $M_x(\mu)$ which appears in Eq. (1) is defined as the flux divided by the chemical potential gradient ($\nabla\mu = \Delta\mu/l$) across the membrane:

$$M_x(\mu) = -\frac{J}{\nabla\mu}, \tag{4}$$

where x is the domain type ($x = S, S', N, M$) and where S and S' are the different subnanoporous domain types and N and M are the nanoporous and macroporous domain types, respectively.

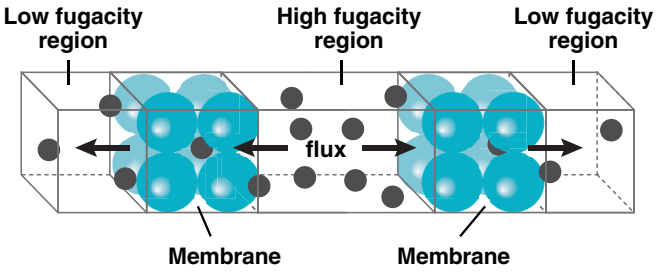

FIG. 2. (Color online) Schematic representation of the DCV-GCMD method. The simulation box consists of two reservoirs (two low-fugacity volumes and one high-fugacity volume, where the chemical potentials are kept constant) and two membranes inserted between the reservoirs. Fluid molecules permeate through the membranes from the high- to the low-fugacity reservoirs.

Membranes in our DCV-GCMD simulations consist of subnanoporous and nanoporous domains. These domains were obtained by placing in a cubic box of a size $a = 2.5$ nm eight nonporous spheres of a radius $r = 1.0$ nm and 0.7 nm, respectively. These domains are referred to as subnanoporous (S) and nanoporous (N) domains in Fig. 1. To test the effect of the subnanoporosity, we also consider subnanoporous domains (S') made up of a disordered porous carbon which consists of a realistic model of active carbon obtained by pyrolizing and activating sucrose [41]. Macroporous domains (M) are assumed to obey bulk transport through the Maxwell-Stefan equation.

The CH_4 molecules, the C and H atoms in the model of disordered porous carbon (CS1000a), and the spheres which form S and N domains are described as simple Lennard-Jones particles (LJ):

$$U(r_{ij}) = 4\epsilon_{ij}\left[\left(\frac{\sigma_{ij}}{r_{ij}}\right)^{12} - \left(\frac{\sigma_{ij}}{r_{ij}}\right)^{6}\right],$$

with parameters shown in Table I. Here r_{ij} is the distance between sites i and j, and σ_{ij} and ϵ_{ij} are LJ parameters deduced from the conventional Lorentz-Berthelot combining rules.

TABLE I. Lennard-Jones potential parameters. The values for methane and the C and H atoms in CS1000a are taken from Ref. [41].

Site type	ϵ (kJ/mol)	σ(Å)
Methane	1.230	3.73
CS1000a carbon	0.232	3.36
CS1000a hydrogen	0.125	2.42
S sphere	12.9981	10.0
N sphere	12.9981	7.0

Based on previous works on molecular adsorption and transport in nanoporous carbons, the domains used in the molecular simulations were chosen to be large enough to avoid finite-size effects, i.e., a few nm (see Ref. [46], for instance). For such large systems, the effect of adsorption and transport at the external interface between the porous solid and the bulk external reservoir can be neglected. In particular, the flux across the porous domain, which results from an external pressure gradient or chemical potential, is independent of the physical state of the external adsorbed fluid. This was demonstrated by Maginn and coworkers [47], who showed that grand-canonical molecular dynamics and nonequilibrium molecular dynamics lead to identical results (we note that nonequilibrium molecular dynamics is performed by applying a pressure gradient to a system without any external interface). The density ρ in a given domain at a pressure P was assumed to be equal to the density of the fluid confined in the middle of the domain (i.e., without considering the effect of the film adsorbed at the external interface). This constitutes an approximation of real systems in which adsorption at the interface between different domain types might affect transport. However, we believe that the present approach is a reasonable first step towards describing multiscale adsorption and transport in complex porous media. In particular, as stated earlier, this approximation is valid for large domains where the effect of adsorption and dynamics at the external surface are negligible compared to phenomena occurring in the domain center.

All molecular simulations were done with LAMMPS [48], which was modified and extended to implement DCV-GCMD simulations. The chemical potential of CH_4 in the reservoirs, which is an input parameter for DCV-GCMD simulations, was estimated using the Widom test particle method as described in Ref. [46]. The dimensions of the simulation cell are $25 \times 25 \times 25$ nm^3: two low-fugacity reservoirs that are 5 nm thick in the x direction (flux direction), two membranes that are 2.5 nm thick (one unit cell), and one central high-density reservoir that is 10 nm thick. To maintain a constant temperature throughout the simulation box, each region is coupled to its own (Nose-Hoover) thermostat with a damping constant of 100 fs. The temperature was then defined by subtracting the streaming velocity from the flux direction of the velocities. The mobility M, which has to be upscaled in the lattice model, was estimated from Eq. (4) using the last 4.5 ns of a 5-ns run.

The mobility M as a function of pressure P (assumed to be equal to the fugacity f, as expected for an ideal gas) is shown in Fig. 3 for the domains S', S, and N. To do so, the upstream and downstream chemical potentials, $\mu_\uparrow$ and $\mu_\downarrow$, were chosen to correspond to $P_\uparrow = 20$, 110, 210, 310 and $P_\downarrow = 10$, 100, 200, 300 bar, respectively. The temperature was set constant at $T = 423$ K. For all domains, M increases upon increasing P. Note that the mobility M decreases with P when expressed as the response to a pressure/fugacity gradient since $\nabla\mu = kT\nabla f/f$.

The simulations of the CH_4 sorption isotherm were obtained using conventional grand-canonical Monte Carlo simulations in which constant chemical potential and temperature are imposed. We checked that such adsorption isotherms can also be obtained using the DCV-GCMD technique, where upstream and downstream chemical potentials are taken equal to each other. To ensure consistency, the same force fields and models were used in the GCMC and MD techniques. The adsorption isotherms for the domains S, S', N, and M are shown in Fig. 4. These curves report the absolute density ρ as a function of the pressure P (given the low-pressure conditions considered in this paper, the chemical potential is readily obtained from the pressure using the ideal gas law). The adsorption isotherm for bulk domains M corresponds to the bulk equation of state of methane at $T = 423$ K. As expected for materials with pores in the range $\sim 0.1-1$ nm, the adsorption isotherms for S, S', and N conform to the Langmuir adsorption isotherm:

$$\rho = \rho_s \frac{bP}{1+bP}, \tag{5}$$

where ρ_s is the density when filling is complete and b is an adsorption constant which describes the affinity of the fluid for the confining host. The absolute density of confined fluid was used throughout this work instead of the excess density. The excess density, which is the apparent density measured in volumetric adsorption measurements, is not corrected for the fact that the gas (i.e., nonadsorbed) phase occupies the porous volume not occupied by the adsorbed phase. As a result, the excess density must be corrected to add the gas contribution to get the absolute density. The latter density, which is necessarily

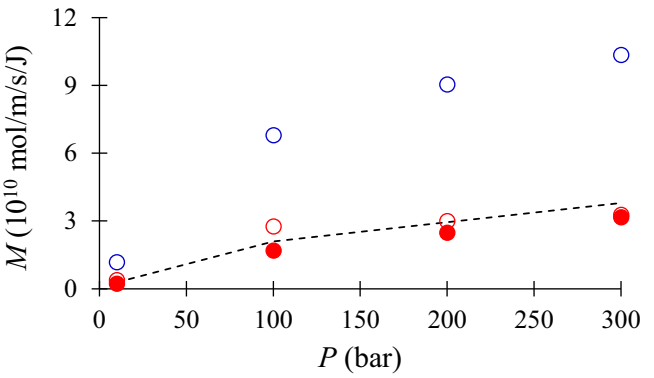

FIG. 3. (Color online) Mobility M as a function of pressure P at $T = 423$ K for the N (blue circles), S (red open circles), and S' (red closed circles) domains. The dashed line corresponds to the Maxwell-Stefan equation for the S' domain. The pressure P is assumed to be equal to the fugacity f, as expected for an ideal gas.

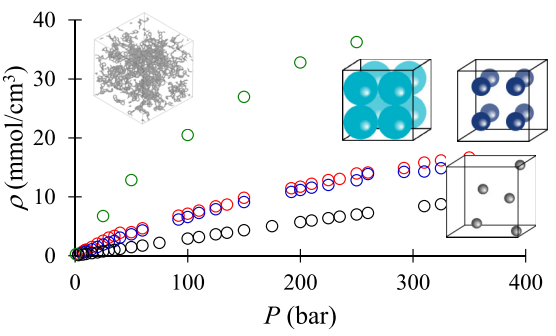

FIG. 4. (Color online) Adsorption isotherms for CH_4 at $T = 423$ K in different domains: S (red), S' (green), N (blue), and M (black).

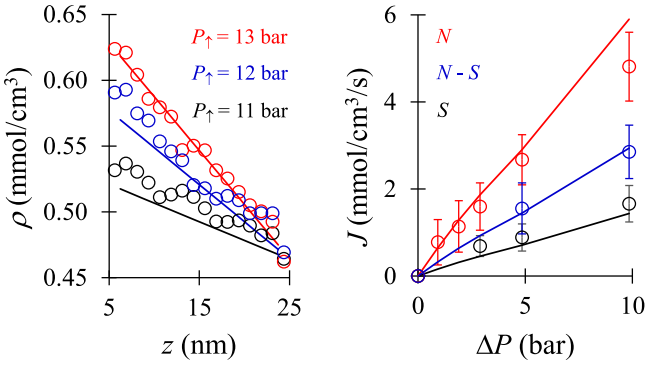

FIG. 5. (Color online) Left: Density profiles $\rho(z)$ of CH_4 flowing at $T = 423$ K in a medium of length L made of domains N: (red) $P_\uparrow = 13$ bar, (blue) $P_\uparrow = 12$ bar, and (black) $P_\uparrow = 11$ bar. In all cases, $P_\downarrow = 10$ bar. The symbols and lines are the molecular simulation and lattice model data. Right: Flux J as a function of ΔP for CH_4 in a medium of a length $L = 20$ nm made of S or N domains only and a random distribution of S and N domains. $P_\downarrow = 10$ bar. The symbols and lines are the molecular simulation and lattice model data.

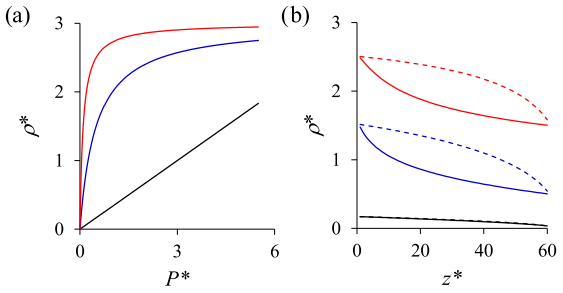

FIG. 6. (Color online) (a) Langmuir adsorption isotherms with $\rho_s = 3$, $b = 2$ (blue line) and $\rho_s = 3$, $b = 10$ (red line). The ideal gas equation of state is also shown for comparison (black line). (b) For each Langmuir adsorption isotherm and the ideal gas law, we calculated the density profile in a membrane of a length $L_z = 60$ when transport is induced by a pressure difference $\Delta P^* = 0.4$ ($P_\uparrow = 0.5$ and $P_\downarrow = 0.1$). The color code is the same as in (a). For each adsorption regime, the effect of density on the mobility coefficient $M(\rho) = k\rho/\eta$ is studied: (solid line) $\eta = \frac{\eta_0}{2}[1 + \exp(c\rho)]$ and (dashed line) $\eta = \eta_0$ for all ρ.

larger than the excess density, reports the total number of molecules in the porosity. The absolute density, which is the density estimated from our molecular simulations (in which all molecules adsorbed in the pores are counted), must be used in our adsorption and transport model as it corresponds to the total number of molecules involved in transport.

D. Validation

The validity of our bottom-up model was first assessed by comparing its predictions against large-scale MD. Figure 5 compares the density profiles obtained from MD and the lattice model across a membrane of a length $L = 20$ nm made of N domains only. For the same $P_\downarrow = 10$ bar, different $\vec{\nabla}\mu$ were considered by varying $P_\uparrow$. Figure 5 also compares the predictions of the lattice model with MD for the flux J as a function of ΔP in membranes made of S and N domains. The two methods are in good agreement (within the error bar), which shows the ability of the lattice model to reproduce results from MD. Note that the data used to validate the lattice model differ from those to calibrate the model (for each domain type x the latter consist of a single domain of length l) so Fig. 5 is a true validation. The flux J in Fig. 5 increases linearly with increasing the pressure gradient, which shows that the confined fluid is in the linear response regime at these P and T.

III. RESULTS

A. Adsorption effect

Our model accounts for adsorption effects on transport. In order to illustrate such adsorption effects, we have compared the predictions of our model for different adsorption regimes. In addition to the simple ideal gas law (no adsorption), which is often invoked to describe gas transport in pores [49], two different Langmuir adsorption isotherms were considered [Fig. 6(a)]. For each regime, we predicted the flow induced by a pressure difference $\Delta P^* = 0.4$ in a membrane of a length $L_z = 60$ made of nanoporous domains only. While this system is necessarily an oversimplification of real systems, it allows us to probe the effect of different adsorption regimes on transport in such porous media. For each adsorption regime, we also investigated the effect of density on the mobility coefficient $M(\rho) = k\rho/\eta$. To do that, we considered a regime in which $M(\rho)$ strongly depends on the density $\{\eta = \frac{\eta_0}{2}[1 + \exp(c\rho)]\}$ and a regime and in which $M(\rho)$ weakly depends on the density $\eta = \eta_0$ for all ρ. Figure 6(b) shows the density profile obtained in the steady state for the different adsorption and mobility regimes. As expected, adsorption strongly affects the density profiles. Moreover, the density dependence of the mobility also affects the density profiles whose curvature can be positive or negative depending on the type of mobility considered. The flow resulting from such effects is also greatly affected by the type of adsorption and mobility considered (the flow decreases by two orders of magnitude as one switches from the ideal gas law to the strongly adsorbing Langmuir regime). Moreover, for a given adsorption regime, the flux J for $\eta = \eta(\rho)$ is always larger than for $\eta = \eta_0$ since $\eta > \eta_0$ for all ρ. These data show that our model captures both the changes in the confined fluid density upon transport and the effect of density on the mobility of the confined phase.

B. Effect of domain heterogeneity

To demonstrate the novel insights that can be gained from our lattice model, we have compared its predictions with Fick's second law (the latter calculations were performed using AVIZO software [50]). The two techniques were compared for an organic-rich shale sample Haynesville, provided by Shell [see Fig. 7(a)]. Two hundred forty images (260 × 632 pixels) with a pixel resolution of 5×5 nm^2 were obtained by means of focused ion beam-scanning electron microscopy [FIB-SEM, Fig. 7(b)]. A segmentation procedure was then performed based on a global threshold method; such a technique assigns a pixel to a given domain type using its gray level. With the aim to determine the number of thresholds, i.e., elementary domain types and their corresponding gray levels, we use the

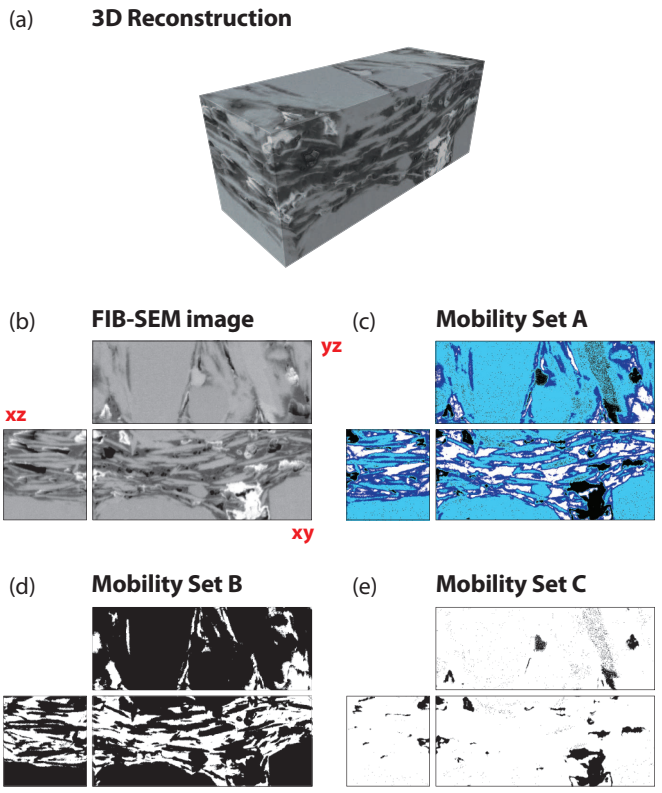

FIG. 7. (Color online) (a) The 3D structural data for an organic-rich gas shale sample (Haynesville shale) as obtained from FIB-SEM. (b) The FIB-SEM data consist of a set of 240 images (260 × 632 pixels) with a pixel resolution of 5 × 5 nm^2. A visualization of the conducting domains for each mobility set is presented in panels (c), (d), and (e). (c) The mobility set A assigns different mobilities for the domain types: $M_S < M_N < M_M$ and $M_I = 0$. The macroporous, nanoporous, subnanoporous, and inorganic domains are shown in white, blue, cyan, and black, respectively. (d) The mobility set B assumes that only the macropores are permeable with a mobility equal to M_M while all other domains are considered impermeable ($M_S = M_N = M_I = 0$). With this mobility set, the macroporous domains are shown in white while all the other domains are shown in black. (e) The mobility set C assumes that the subnanopores, nanopores, and macropores have the same mobility $M_M = M_N = M_S$ while all the inorganic domains are impermeable ($M_I = 0$). The conducting domains (macropores, nanopores, and subnanopores) are shown in white while the inorganic domains are in black.

minimum histogram approach [51]. In this method a histogram is first constructed by grouping the pixels with the same intensity from 0 to 255. The number of thresholds is then determined by counting all the local minima of the histogram, and their locations correspond to the threshold values. We have thus identified two thresholds with the values of 104 and 171. Based on these data we have segmented the images into four domain types: (1) pixels with an intensity larger than 171 are considered as impermeable inorganic matter (clays, quartz, pyrite, etc.); (2) pixels with an intensity between 104 and 171 are subnanoporous domains; (3) an isolated pixel ($\sim 5 \times 5 \times 5\,\text{nm}^3$) with an intensity smaller than 104 is considered a nanoporous domain, and (4) a group of pixels (whose size is therefore larger or equal to 10 nm in at least one direction) with an intensity smaller than 104 is considered a macropore.

TABLE II. Normalized flux along the x, y, and z directions for the shale sample shown in Fig. 7(a). Results are presented for the different mobility sets considered in Figs. 7(c)–7(e). For each mobility set, both the results from the lattice model (LM) and the finite-volume method (FV) consisting of solving Fick's law are shown. The latter is only suitable for binary systems (i.e., a set of conducting or isolating domains).

Segmentation	J_x/J_{bulk}		J_y/J_{bulk}		J_z/J_{bulk}	
type	LM	FV	LM	FV	LM	FV
A	0.09	n/a	0.25	n/a	0.28	n/a
B	0.04	0.04	0.22	0.21	0.25	0.25
C	0.85	0.82	0.90	0.85	0.91	0.90

In order to validate our lattice model, the flux of methane was determined in the x, y, and z directions for the shale sample shown in Fig. 7(a) using our lattice model and Fick's second law. We considered pressure and temperature conditions which are relevant to shale gas recovery: $T = 423$ K, $P_\uparrow = 11$ bar, and $P_\downarrow = 10$ bar. Under these conditions the fluid flow is known to be diffusive and can be conveniently described by Fick's law. For each direction, the normalized flux J_a/J_{bulk} ($a = x, y, z$) is defined as the ratio of the flux through the porous medium J and the flux in the absence of porous medium J_{bulk} (the latter is computed by using the lattice model and the numerical solution of Fick's law on the same grid but with all sites accessible to the fluid). Different mobility sets M_x for the four domain types x were compared: subnano-, nano-, macroporous, and inorganic domains (Fig. 7 and Table II). When assigning the same transport coefficients M_x to the conducting porous domains (all domains except inorganic domains), our lattice model predicts fluxes that are in agreement with Fick's law. This result, obtained for mobility sets that neglect the effect of small porosity scales on transport, shows that our model is consistent with conventional approaches. The comparison between the different mobility sets shows that the effect of confinement in the pores <10 nm affects the flow in multiscale media; by assuming the same M_x for subnano-, nano-, and macroporous domains, Fick's law overestimates the flux. On the other hand, the data for the different mobility sets demonstrate that the flow through the subnanoporous domains, often inaccessible or neglected in fluid simulators, significantly contributes to the flux. This also suggests that the Katz-Thompson model [52,53], which assumes that flow occurs through the percolating network of largest pores as probed by Hg intrusion (>10 nm), necessarily fails for media with subnano- and nanopores. The results for the three considered mobility sets are presented in Table II. Both calculation types show that the sample considered is far from being representative since fluid transport is anisotropic (the flux in the direction x being much smaller than in the directions y and z). As expected, for the mobility sets B and C, which assign the same mobility to different conducting porous domains, our lattice model predicts fluxes that are in good agreement with those obtained from Fick's law. This result, which was obtained for systems (i.e., mobility sets) that neglect

the effect of small porosity scales on transport (since small pores are assumed to conduct as efficiently as macroporous domains), shows that our lattice model is consistent with conventional approaches of transport in porous media. The comparison between the mobility sets A and C shows that the severe effect of confinement in the subnanopores and nanopores (which make their mobility much smaller than in the macropores) drastically affects the flow predictions for multiscale porous media; by assuming the same mobility coefficient for subnanoporous, nanoporous, and macroporous domains, the transport calculations for the mobility set C overpredicts by a factor from 3 to 10 the flow predicted with the mobility set A. Moreover, the use of the same mobility coefficients for the different conducting domains (mobility set C) leads to underestimated anisotropy effects in predicting the transport properties of a given sample. Indeed, by using the same mobility coefficient for the subnanoporous, nanoporous, and macroporous domains, the mobility set C adopts a sample description that is much more homogeneous and isotropic. Consequently, the resulting flow properties are much larger (because this mobility set overestimates transport in the smallest domains by assigning them the mobility of the macroporous domains) and do not reflect the strong anisotropy of the sample. More interestingly, the comparison between the mobility sets A and B demonstrates that the flow through the subnanoporous domains, which are often inaccessible or neglected in fluid simulators, significantly contributes to the total flux. This result shows that large errors are to be expected if crude approximations are used such as (1) using pore scale independent mobility coefficients and (2) neglecting transport through the smallest porosity scales. In particular, such discrepancies between the different approaches and approximations could explain large errors in the predicted transport properties for tight rocks and unconventional reservoirs such as gas shales, and so on. This result further justifies the development of the simple multiscale model reported in this work, which allows us to take into account the effects of pore size and of adsorption on transport in complex, disordered media.

C. Multiscale transport

Transport in porous media is often described using the following empirical equation [54]:

$$J = \frac{\phi}{\tau} J_0, \tag{6}$$

which relates the flux J to the porosity ϕ and tortuosity τ of the medium and the flux J_0 in the absence of medium. While ϕ can be assessed using adsorption experiments, τ and J_0 are often determined using NMR. To discuss the validity of Eq. (6), the lattice model was used to predict transport in media made up of random assemblies of subnano- and nanoporous domains (the former are S or S' domains). Figure 8 shows the flux J for $\Delta P = 1$ bar as a function of the porosity ϕ ($\phi = \sum_i \phi_i / N_d$ where the sum is over the N_d domains of the medium and ϕ_i is the porosity of domain i). Two membrane sizes, 20 nm and 1 μm, were considered. Figure 8 also shows the results for a much larger membrane (400 μm); for this system, the data for the system with 1 μm were upscaled by assuming that a domain

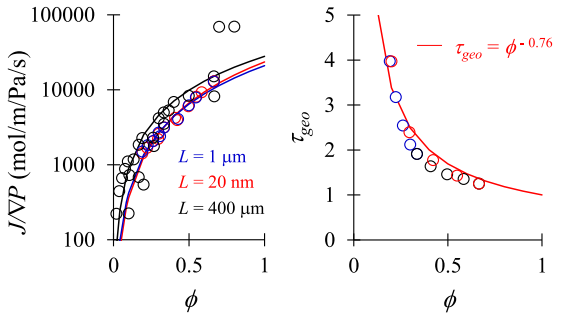

FIG. 8. (Color online) Left: Flux J versus porosity ϕ for systems with different porosity scales. Red and blue symbols are for systems with different lengths. The black data are for a much larger system (400 μm) and were obtained by upscaling the data for the system with 1 μm. $P_\uparrow = 11$ bar and $P_\downarrow = 10$ bar, $T = 423$ K. The lines are fits with ϕ^m. Right: Geometrical tortuosity τ_{geo} as a function of porosity ϕ for media made of different domains: S'/N (red circles), S'/S (blue circles), and S/N (black circles). The line is a fit with ϕ^{-n} ($n = 0.76$).

in the larger lattice is the entire lattice for the smaller system. In agreement with Eq. (6), Fig. 8 shows that J increases upon increasing ϕ. In fact, $J \sim \phi^m$ with $m \sim 1.5-1.8$, showing that our model allows recovering Archie's empirical law [20]. Our model therefore provides a theoretical framework for this empirical relation as the power law is in no way imposed. In contrast, we recall that Archie's law and its linear response to ∇P are valid for certain ϕ and P ranges only [55].

Comparison between $J \sim \phi^m$ obtained using the lattice model and Eq. (6) suggests that $\tau \sim \phi^{1-m}$. To check this scaling behavior and the validity of Eq. (6), the tortuosity τ was estimated for different porous media. We write that $\tau = \tau_{geo}\tau_{ads}$ is the product of a geometrical tortuosity τ_{geo}, independent of the fluid, and an adsorption tortuosity τ_{ads} which depends on the fluid-surface interaction. In other words, the tortuosity τ, the transport resistance of a given fluid (related to the reciprocal of the permeability k), is the combination of a geometrical contribution (intrinsic material property) and a contribution from adsorption and confinement. τ_{geo} is estimated by mapping the medium on a grid where each node belongs to the pore space or solid matrix based on its distance d to the closest solid particle; if d is larger than the particle radius, the node is accessible to fluid molecules. Random-walk simulations are then used to quantify the average path length $\tilde{L}$ to cross the sample between opposite sides [56]. τ_{geo} is defined as $\tilde{L}/L_0$, where L_0 is the path length in the absence of solid. While several definitions are possible for τ_{geo}, this method is consistent with NMR experiments in which τ is the diffusion formation factor. Figure 8 shows τ_{geo} as a function of ϕ for different systems. τ_{geo} tends to 1 as $\tau_{geo} = \phi^{-0.76}$. This power law, obtained from independent estimates of τ_{geo}, is consistent with the lattice results above interpreted in the framework of Eq. (6), i.e., $\tau \sim \phi^{1-m}$ with $m \sim 1.5-1.8$. In addition to validating Eq. (6) for multiscale transport, these results validate *a posteriori* that τ is the product of a geometrical τ_{geo} and an adsorption τ_{ads} contributions. In particular, the results above show that τ_{ads} is weakly dependent on ϕ, which is consistent with its definition as being the nongeometric contribution. This

weak ϕ dependence is thought to be less valid with increasing fluid-solid interaction as the system becomes more sensitive to the surface to volume ratio and porosity.

IV. CONCLUSION

This work demonstrates the potential application of our model to transport in multiscale media by rigorously including the adsorption-transport interplay at different scales. This method differs from coarse-grained models as adsorption and dynamics are coupled and upscaled through the use of a common thermodynamic variable (chemical potential). By using a lattice model in which adsorption and transport at a given scale can be incorporated, our model upscales information at a lower scale across several scales. This bottom-up approach, which allows us to upscale results from molecular simulation, with no assumption about the adsorption and flow regimes, allows us to recover empirical equations such as Archie's law. This model also shows that the tortuosity τ can be expressed as a geometrical contribution, easily assessed from structural data, multiplied by an adsorption contribution weakly dependent on ϕ. The present model provides a theoretical framework for transport-permeability experiments in multiscale media such as hierarchical materials, geological media, and artificial and biological membranes. In particular, this model offers a novel tool to address transport in very low permeable media such as gas shales (which cannot be described using conventional simulators) but is also relevant to other multiscale media. This approach does not include turbulence and therefore should be used for low Reynolds numbers [57]. Improvements include considering nonlinear responses and solid deformations upon adsorption or transport. The present model can also be extended to include phase transitions and account for transport discontinuity or hystereses.

ACKNOWLEDGMENTS

This work has been carried out within the French Investissements d'Avenir (ICoME2/ANR-11-LABX-0053 and A*MIDEX/ANR-11-IDEX-0001-02). We acknowledge financial and technical support from Schlumberger and Shell through the X-Shale project. FIB-SEM data of shale were provided by R. Hofmann (Shell). Stimulating discussions with L. Bocquet are gratefully acknowledged.

[1] P. J. M. Monteiro, C. H. Rycroft, and G. I. Barrenblatt, Proc. Natl. Acad. Sci. USA **109**, 20309 (2012).
[2] R. J. M. Pellenq, A. Kushima, R. Shahsavari, K. J. Van Vliet, M. J. Buelher, S. Yip, and F. J. Ulm, Proc. Natl. Acad. Sci. USA **106**, 16102 (2009).
[3] T. W. Patzek, F. Male, and M. Marder, Proc. Natl. Acad. Sci. USA **110**, 19731 (2013).
[4] F. Civan, *Porous Media Transport Phenomena* (Wiley, New York, 2011).
[5] M. Knudsen, Ann. Phys. (Leipzig) **333**, 75 (1909).
[6] S. Gruener and P. Huber, Phys. Rev. Lett. **100**, 064502 (2008).
[7] L. J. Klinkenberg, in *Drilling and Production Practice* (American Petroleum Institute, Washington, DC, 1941), pp. 200–213.
[8] M. Cieplak, J. Koplik, and J. R. Banavar, Phys. Rev. Lett. **86**, 803 (2001).
[9] B. Coasne, A. Galarneau, R. J. M. Pellenq, and F. Di Renzo, Chem. Soc. Rev. **42**, 4141 (2013).
[10] L. Bocquet and E. Charlaix, Chem. Soc. Rev. **39**, 1073 (2010).
[11] S. T. O'Connell and P. A. Thompson, Phys. Rev. E **52**, R5792(R) (1995).
[12] J.-F. Bourgata, P. Le Tallec, and M. Tidriri, J. Comp. Phys. **127**, 227 (1996).
[13] V. B. Shenoy, R. Miller, E. B. Tadmor, R. Phillips, and M. Ortiz, Phys. Rev. Lett. **80**, 742 (1998).
[14] M. Levesque, M. Duvail, I. Pagonabarraga, D. Frenkel, and B. Rotenberg, Phys. Rev. E **88**, 013308 (2013).
[15] K. Balasubramanian, F. Hayot, and W. F. Saam, Phys. Rev. A **36**, 2248 (1987).
[16] B. Albaalbaki and R. Hill, Proc. R. Soc. A **468**, 3100 (2012).
[17] C. C. Mei, Transp. Porous Med. **9**, 261 (1992).
[18] D. Cioranescu and P. Donato, *An Introduction to Homogenization* (Oxford University Press, Oxford, 1999).
[19] R. Valiullin, S. Naumov, P. Galvosas, J. Kaerger, H. J. Woo, F. Porcheron, and P. Monson, Nature **443**, 965 (2006).
[20] G. E. Archie, Phys. Trans. AIME **146**, 54 (1942).
[21] P. W. J. Glover, Geophys. **75**, E247 (2011).
[22] S. Plimpton, Comput. Mater. Sci. **4**, 361 (1995).
[23] N. G. Hadjiconstantinou and A. T. Patera, Int. J. Mod. Phys. **8**, 967 (1997).
[24] E. G. Flekkoy, G. Wagner, and J. Feder, Europhys. Lett. **52**, 271 (2000).
[25] X. B. Nie, S. Y. Chen, and M. O. Robbins, J. Fluid. Mech. **500**, 55 (2004).
[26] S. Li and D. Qian, *Multiscale Simulations and Mechanics of Biological Materials* (Wiley, New York, 2013).
[27] S. Chen and G. D. Doolen, Annu. Rev. Fluid Mech. **30**, 329 (1998).
[28] D. Noble and J. Torczynski, Int. J. Mod. Phys. C **9**, 1189 (1998).
[29] Y. L. Chen, X. D. Cao, and K. Q. Zhu, J. Non-Newtonian Fluid Mech. **159**, 130 (2009).
[30] P. J. Hoogerbrugge and J. M. V. A. Koelman, Europhys. Lett. **19**, 155 (1992).
[31] M. A. D. Viera, P. Sahay, M. Coronado, and A. O. Tapia, *Mathematical and Numerical Modeling in Porous Media: Applications in Geosciences* (Taylor & Francis, London, 2012).
[32] A. Raoof, Ph.D. thesis, Utrecht University, 2011.
[33] S. Whitaker, *The Method of Volume Averaging* (Kluwer, Amsterdam, 1999).
[34] I. Battiato and D. M. Tartakovsky, J. Contam. Hydrol. **120-121**, 18 (2011).
[35] A. M. Tartakovsky, D. M. Tartakovsky, T. D. Scheibe, and P. Meakin, SIAM J. Sci. Comput. **30**, 2799 (2008).
[36] J. Chu, B. Engquist, M. Prodanovic, and R. Tsai, Multiscale Model. Simul. **10**, 515 (2012).
[37] J. A. White, R. I. Borja, and J. T. Fredrich, Acta Geotechnica **1**, 195 (2006).

[38] M. A. Diaz Viera, P. Sahay, M. Coronado, and A. O. Tapia, *Mathematical and Numerical Modeling in Porous Media: Applications in Geosciences* (CRC Press, Boca Raton, FL, 2012).
[39] H. Brenner, *Transport Processes in Porous Media* (McGraw-Hill, New York, 1987).
[40] Other techniques such as nonequilibrium molecular dynamics can be used to estimate $M_x(\mu)$ in Eq. (1).
[41] S. K. Jain, R. J. M. Pellenq, J. P. Pikunic, and K. E. Gubbins, Langmuir **22**, 9942 (2006).
[42] S. Torquato, *Random Heterogeneous Materials: Microstructure and Macroscopic Properties* (Springer, Berlin, 2011).
[43] F. Capuani, I. Pagonabarraga, and D. Frenkel, J. Chem. Phys. **121**, 973 (2004).
[44] G. S. Heffelfinger and F. van Swol, J. Chem. Phys. **100**, 7548 (1994).
[45] J. M. D. MacElroy, J. Chem. Phys. **101**, 5274 (1994).
[46] A. Boţan, R. Vermorel, F. Ulm, and R. Pellenq, Langmuir **29**, 9985 (2013).
[47] G. Arya, H.-C. Chang, and E. J. Maginn, J. Chem. Phys. **115**, 8112 (2001).
[48] S. Plimpton, J. Comp. Phys. **117**, 1 (1995).
[49] Z. P. Bazant, M. Salviato, V. T. Chau, H. Viswanathan, and A. Zubelewicz, J. Appl. Mech. **81**, 101010 (2014).
[50] AVIZO 3D software [http://www.fei.com/software/avizo3d/]
[51] M. Salzer, A. Spettl, O. Stenzel, J. Smatt, M. Linden, I. Manked, and V. Schmidt, Mater. Charact. **69**, 115 (2012).
[52] A. J. Katz and A. H. Thompson, Phys. Rev. B **34**, 8179 (1986).
[53] A. J. Katz and A. H. Thompson, J. Geophys. Res. **92**, 599 (1987).
[54] P. M. Adler, *Porous Media: Geometry and Transports*, Butterworth-Heinemann Series in Chemical Engineering (Butterworth-Heinemann, London, 1992).
[55] R. B. Pandey and J. F. Gettrust, Phys. Rev. E **80**, 011130 (2009).
[56] P. Epicoco, B. Coasne, A. Gioa, P. Papet, I. Cabodi, and M. Gaubil, Acta Mater. **61**, 5018 (2013).
[57] $\mathrm{Re} = L v_f / v$, where L is the pore diameter, v_f the mean fluid velocity, and v the kinematic viscosity. Using $v_f \sim$ cm/s and $v \sim 10^{-6}\,\mathrm{m}^2/\mathrm{s}$ for methane and water, turbulent flows are observed for $L > 0.1$ m ($\mathrm{Re} > 1000$).